

Supporting Information

Stoichiometric Gradient Rebalancing Achieves Surface Reconstruction and Bulk Homogenization in High-Performance Vapor-deposited Perovskite Solar Cells

Changyu Duan,^a Yichen Dou,^a Shenghan Hu,^a Xinyu Deng,^a Meichen Liu,^a Mengjun Liu,^a Guijie Liang,^{*b} Yong Peng,^a Yi-Bing Cheng^{a, c} and Zhiliang Ku^{*a}

^a *State Key Laboratory of Advanced Technology for Materials Synthesis and Processing, Wuhan University of Technology, Wuhan 430070, Hubei Province, China*

^b *Hubei Key Laboratory of Low Dimensional Optoelectronic Material and Devices, Hubei University of Arts and Science, Xiangyang 441053, Hubei Province, China*

^c *Xianhu Laboratory of the Advanced Energy Science and Technology Guangdong Laboratory, Foshan 528200, Guangdong Province, China*

* Corresponding authors.

E-mail addresses: guijie-liang@hbuas.edu.cn, zhiliang.ku@whut.edu.cn (Z. Ku).

Experimental Section

Materials.

Lead iodide (PbI₂, 99.999%), lead chloride (PbCl₂, 99.999%) and FK209 (98%) were all purchased from Xi'an Yuri Solar Co., Ltd. Formamidinium iodide (FAI, 99.9%), and 2,2',7,7'-Tetrakis[*N,N*-di(4-methoxyphenyl)amino]-9,9'-spirobifluorene (spiro-OMeTAD, 99.9%) were purchased from Advanced Election Technology Co., Ltd. Tin(II) chloride dihydrate (SnCl₂·2H₂O, 99.995%), 4-*tert*-Butylpyridine (*t*BP, 98%), Bis(trifluoromethane)sulfonimide lithium salt (Li-TFSI, 99%), urea (99.5%) and chlorobenzene (CB, 99.8%) were obtained from Sigma Aldrich. Other materials were purchased from Alfa-Aesar or Sigma Aldrich. All chemicals were used as received without further purification.

Perovskite film fabrication

Pristine film. The pristine film was fabricated in a two-step vacuum deposition. In the first step (PbI₂ evaporation), 350 nm PbI₂ films were deposited on glass/FTO/SnO₂ substrates via thermal evaporation at a rate of 3–4 Å s⁻¹. The evaporation process was conducted in a glovebox-integrated chamber under a pressure of 8 × 10⁻⁴ Pa. In the second step (vapor-solid reaction), the as-deposited PbI₂ films were transferred to a custom-built chamber for vapor-solid reaction with FAI vapor. The FAI vapor was generated by heating a glass substrate pre-coated with an ultrasonically sprayed FAI solution (343.9 mg of FAI in 20 mL ethanol). The reaction was carried out at 160°C under a controlled pressure of 100 Pa, allowing the FAI to sublime from the glass substrate and react with the PbI₂ film, as reported in our previous work ¹.

Stoichiometric Gradient Rebalancing (SGR) film. The SGR film was fabricated on the basis of the pristine film. Pure PbI₂ or a combination of PbI₂ and PbCl₂ was deposited onto the pristine perovskite film via thermal evaporation. The deposition rates were maintained at 0.5 Å s⁻¹, with PbI₂ thicknesses of 1, 5, 15, and 50 nm. For the combined PbI₂ and PbCl₂ films, the thickness ratios were 10:1, 5:1, and 2:1. Immediately after evaporation, the films were transferred to a hot plate for further reaction at temperatures of 100, 120, 140, 160, and 180°C for durations of 0.5 min, 1 min, 3 min, and 5 min.

Device fabrication

Small area solar cell. Initially, the FTO glass was etched using a femtosecond laser machine. Substrates were then cleaned sequentially in detergent, deionized water, acetone, and isopropanol, and then dried with compressed dry-air. SnO₂ layers were deposited by chemical bath deposition (CBD) method.² The FTO/SnO₂ substrates were cleaned with ultraviolet ozone for 15 min before use. Pristine and SGR perovskite films were fabricated by the method described above. 73 g of spiro-OMeTAD were dissolved in 1 mL of chlorobenzene, followed by the addition of 30 μL of *t*BP, 18 μL of Li-TFSI solution (520 mg mL⁻¹ in acetonitrile) and 29 μL of FK 209 solution (300 mg mL⁻¹ in acetonitrile). The spiro-OMeTAD solution was spin-coated on perovskite films at 3000 rpm for 30 s in a N₂-filled glove box. Finally, 80 nm of Au electrode was deposited by thermal evaporation under a pressure of 8.0×10^{-5} Pa.

Large-area solar module. Laser etching is a key step in module fabrication. Femtosecond laser (Hongtuo TCR-1030, Wuhan) is used to etch P1, P2 and P3. First, the washed FTO glass is etched P1 through the femtosecond laser. After deposition of SnO₂, perovskite layer and spiro-OMeTAD layer, P2 is formed by laser etching. Finally, it formed effective series-connected modules by etching Au to form P3 lines.

Characterizations

Photovoltaic performance characterization. The *J-V* characteristics and steady-state power output of photovoltaic devices were collected through Keithley 2400 Source Meter in the clean room (approximately 25°C and 25% RH). The light source was a solar simulator (Oriel 94023 4A, 300 W) to match AM 1.5 G. The intensity of the light was 100 mW cm⁻² calibrated by a standard silicon reference solar cell (Oriel, VLSI standards). The forward *J-V* scans were measured from forward -0.1 V to 1.2 V and the reverse scans were from 1.2 V to -0.1 V, at a scan rate of 100 mV s⁻¹ (voltage step of 10 mV and dwell time of 100 ms). The active areas were defined by a black metal aperture with a mask area of 0.1475 cm² or 1 cm², and 10 cm² for the 5 × 5 cm² perovskite solar cell modules. The external quantum efficiency (EQE) was measured by the EQE measurement system (QEX10, PV Measurements, Inc.).

Scanning electron microscopy (SEM). The SEM images were obtained by Hitachi S-4800 or ZEISS Sigma 300.

Time of flight secondary ion mass spectrometry (ToF-SIMS). The depth profiling was conducted using a TOF-SIMS instrument (IONTOF M6) with Bi ions at 30 keV, an ion current of 0.43 pA, and a raster size of 100 $\mu\text{m} \times 100 \mu\text{m}$.

X-ray photoelectron spectroscopy (XPS). The XPS measurements were performed using a Thermo Fisher ESCALAB 250Xi instrument. The binding energy scale was periodically calibrated using a standard gold foil sample (Au 4f_{7/2} peak at 84.0 eV). A monochromatic Al K α X-ray source (1486.6 eV) was operated at 150 W power with a beam spot size of 500 μm . Charge neutralization was applied. The acquired spectra were normalized using the instrument's built-in transmission function correction curve, which was pre-calibrated with standard Ag and Au reference samples. For XPS semi-quantitative analysis, the Scofield sensitivity factor library was used, and background fitting was performed using the Smart-type fitting function in the data analysis software.

Ultraviolet photoelectron spectroscopy (UPS). The UPS measurements were performed using a Thermo Fisher ESCALAB 250Xi instrument. A helium discharge lamp with an excitation energy of 21.22 eV (He I line) was employed as the ultraviolet source. To enhance the detection of low-energy secondary electrons, a negative bias voltage of -5 V was applied to the sample during the measurement of the secondary electron cutoff edge. The Fermi edge position was calibrated using a clean Au reference sample.

Grazing incidence X-ray diffraction (GIXRD). The GIXRD patterns were collected with a Rigaku SmartLab SE diffractometer using Cu K α radiation ($\lambda = 1.54 \text{ \AA}$) as the X-ray source under operation conditions of 40 kV and 150 mA.

Grazing-incidence wide-angle X-ray scattering (GIWAXS). The GIWAXS measurements were conducted with Xenocs Xeuss 3.0 equipped with Eiger2 R 1M hybrid photon counting detectors. The X-ray energy was 8.05 keV and the wavelength was 1.54189 \AA . The distance from the sample to the detector was 100 mm. The incident angle was 0.5°, selected according to our previous reporting.³ Each sample was exposed twice, and the detector moved a certain distance between exposures to eliminate the effects of gaps in the detector.

Residual Stress Measurement (Multi-tilt Angle XRD). The residual stress was measured by Bruker D8 Discover diffractometer, with high-flux microbeam light source, Co K α radiation, wavelength 1.78897 Å, operating voltage 40 kV, current 0.5 mA

Transient absorption spectroscopy (TAS). The TAS was performed using a 1 kHz, 85 fs Ti:sapphire ultrafast laser amplifier with the pump-probe transient absorption spectrometer (Helios), and the wavelength of pump laser is 400 nm under pump power of 5 μ W.

Stability test. Long-term aging stability tests follow the ISOS-D-1 protocol. All devices are stored in environmental test chamber (\sim 25°C, 60 \pm 5% RH). The thermal stability tests (ISOS-D-2I protocol) were carried out in a nitrogen glove box, and the encapsulated devices were put on a hot-plate with a temperature of 85°C. All the devices were cooled down before J - V test. The MPP tracking (ISOS-L-1 protocol) tests were conducted under 1-sun-equivalent white LED illumination in an ambient atmosphere (\sim 25°C, 40–60% RH), and all devices were encapsulated.

Other characterizations. The steady-state PL and Time-resolved photoluminescence (TRPL) spectra were measured by using a 478 nm light pulse from Delta Flex Flux Fluorescence Lifetime System (HORIBA). The excitation laser intensity is 2 mW. The ultraviolet photoelectron spectroscopy (UPS) measurements were performed using a Thermo Fisher ESCALAB 250Xi instrument. The space-charge limited current (SCLC) devices were fabricated with the structure of FTO/SnO₂/perovskites/PCBM/Ag and measured under dark at room temperature with EC-lab (SP300, Bio-Logic).

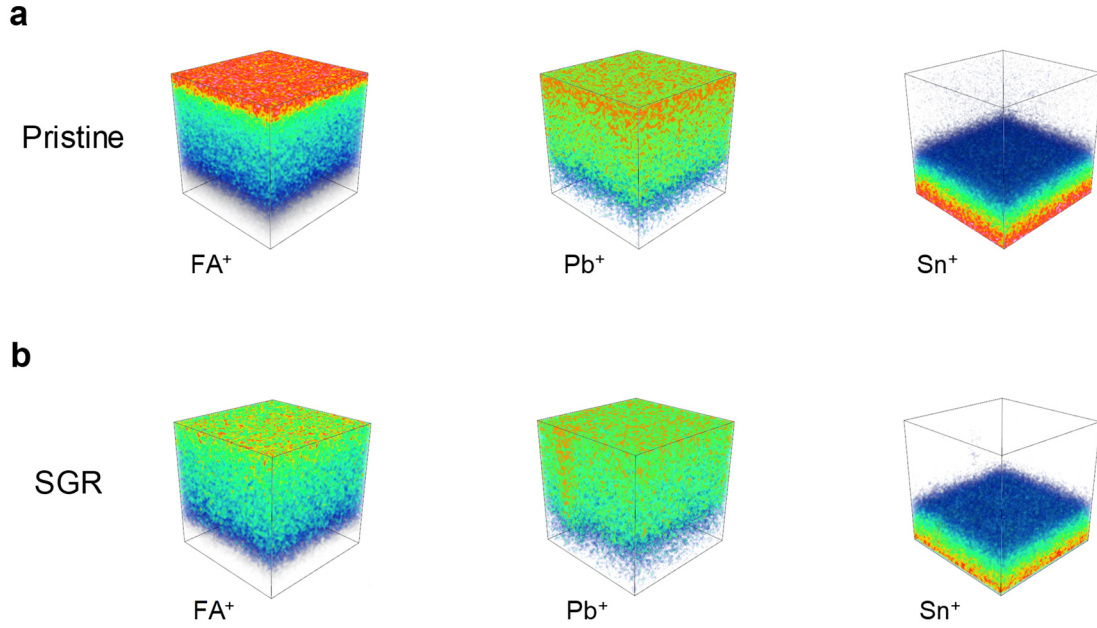


Fig. S1. TOF-SIMS of FA⁺, Pb, and Sn ions in the (a) pristine perovskite film and (b) SGR perovskite film. (measurement area 100 mm by 100 mm).

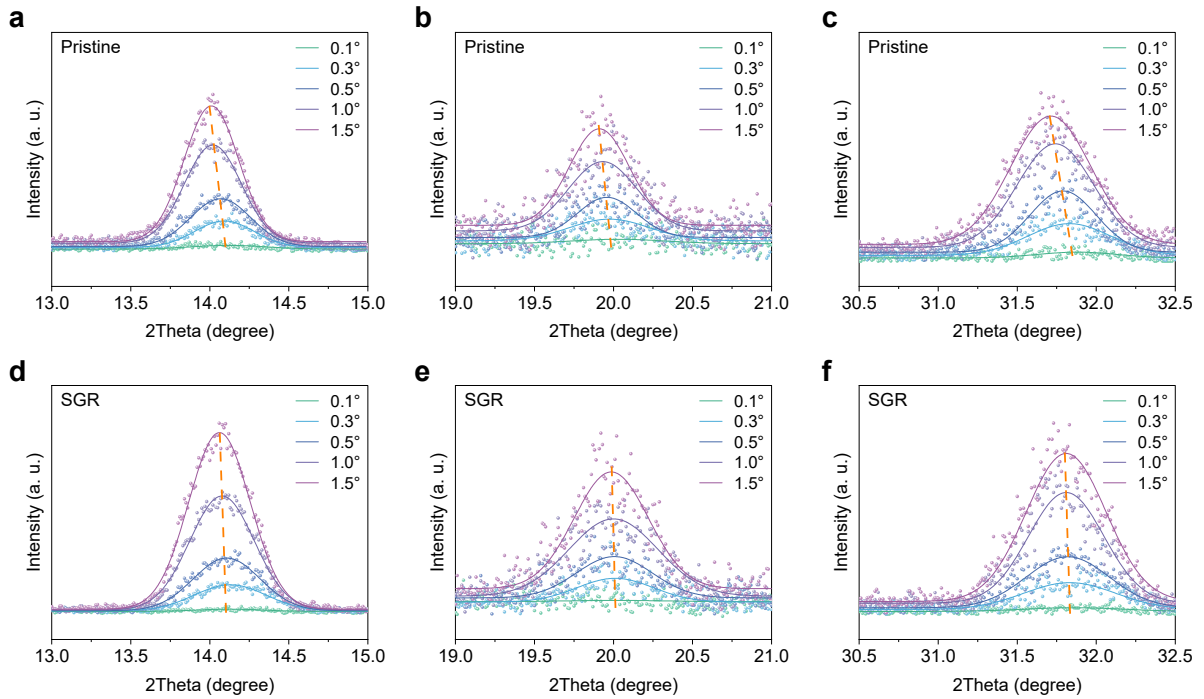


Fig. S2. Localized GIXRD patterns of (a-c) pristine and (d-f) SGR perovskites under varying grazing incidence angles (0.1°, 0.3°, 0.5°, 1.0°, 1.5°).

As-deposited PbI_2 -perovskite composite films

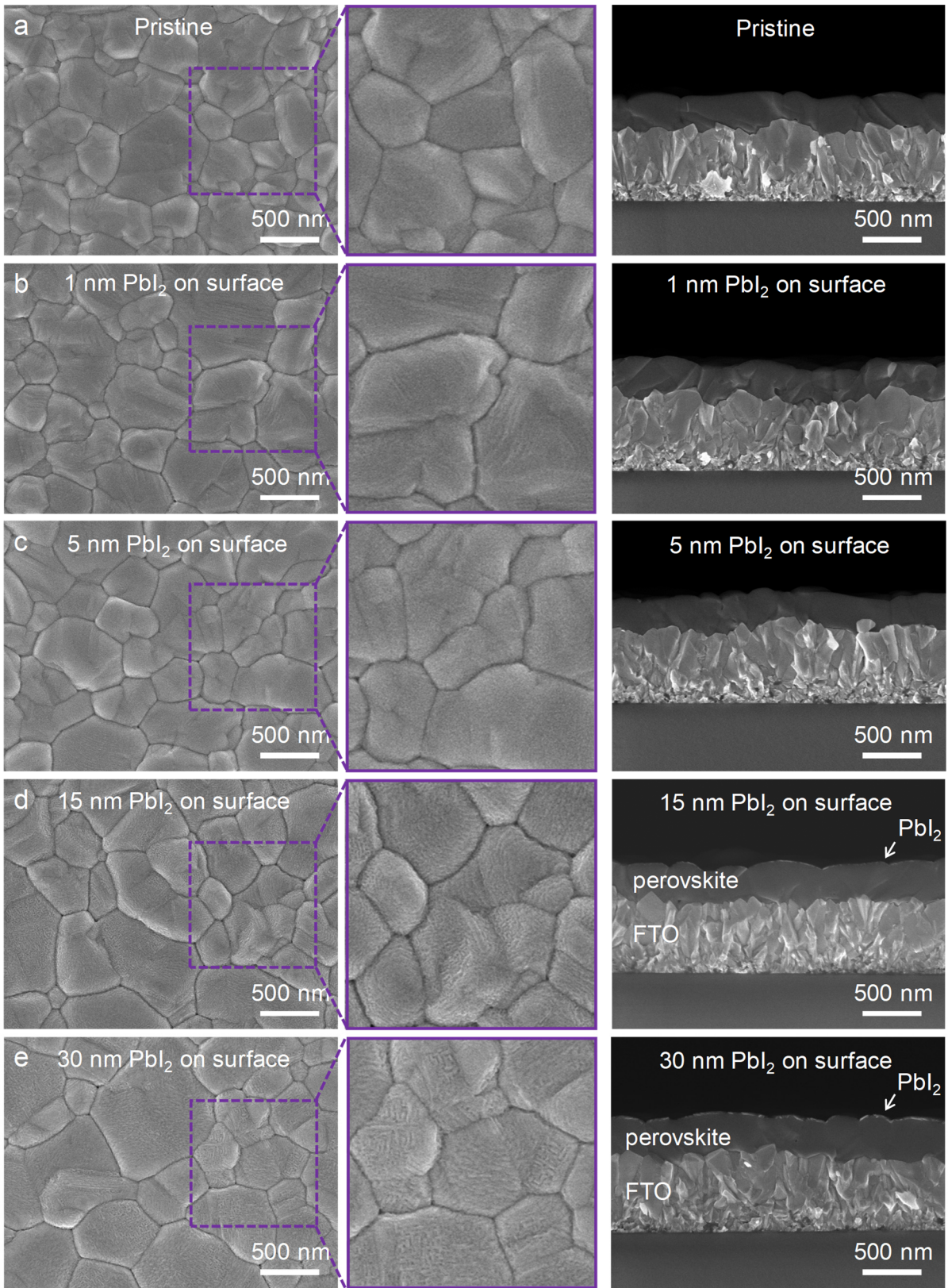


Fig. S3. Surface and cross-sectional SEM images of (a) Pristine perovskite films and (b-e) perovskite films with thermally evaporated PbI_2 surface layers of varying thicknesses (1, 5, 15, 30 nm).

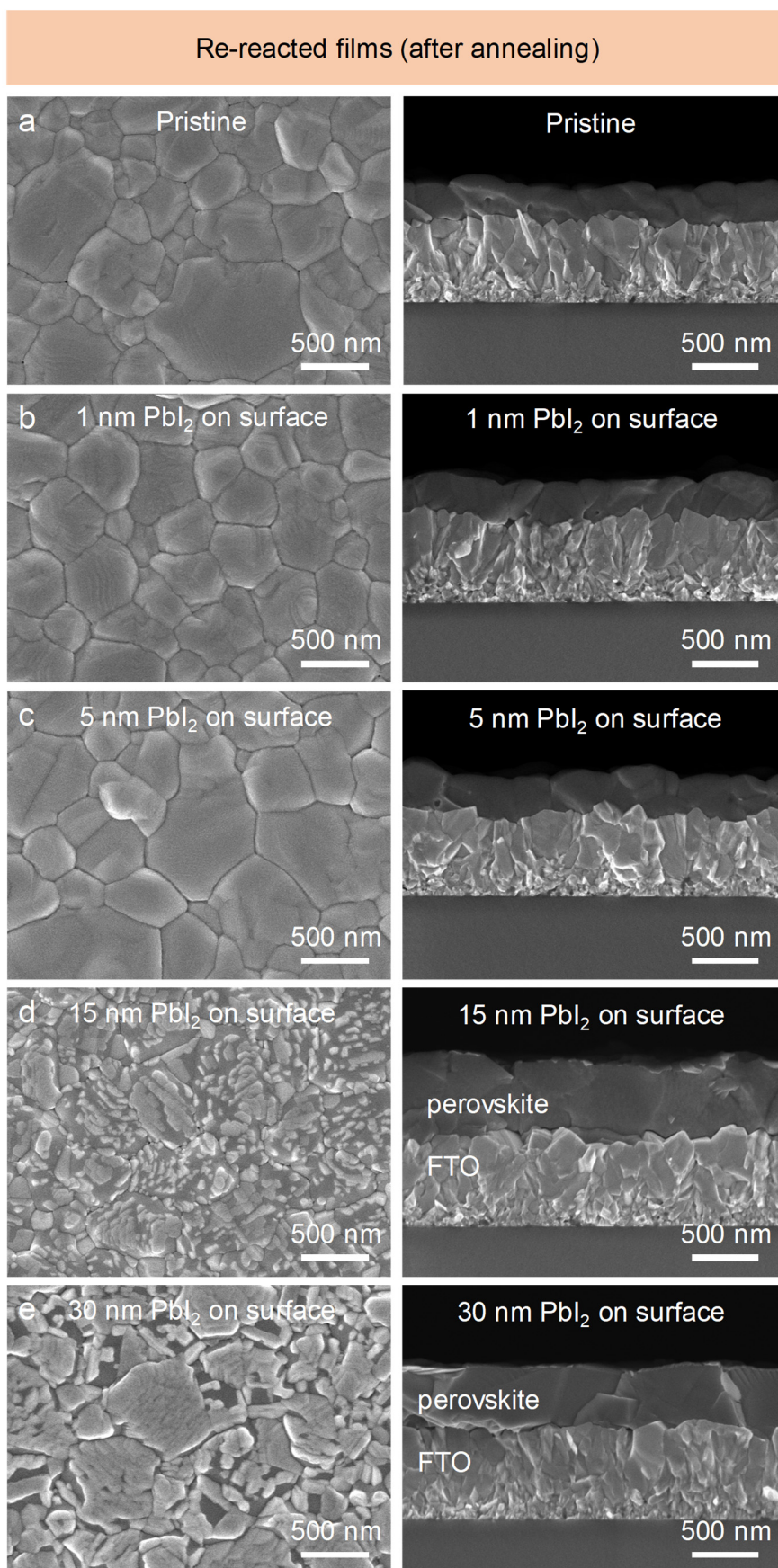


Fig. S4. Surface and cross-sectional SEM images of re-reacted (a) pristine perovskite films and (b-e) SGR perovskite films with PbI_2 surface layers of varying thicknesses (1, 5, 15, 30 nm).

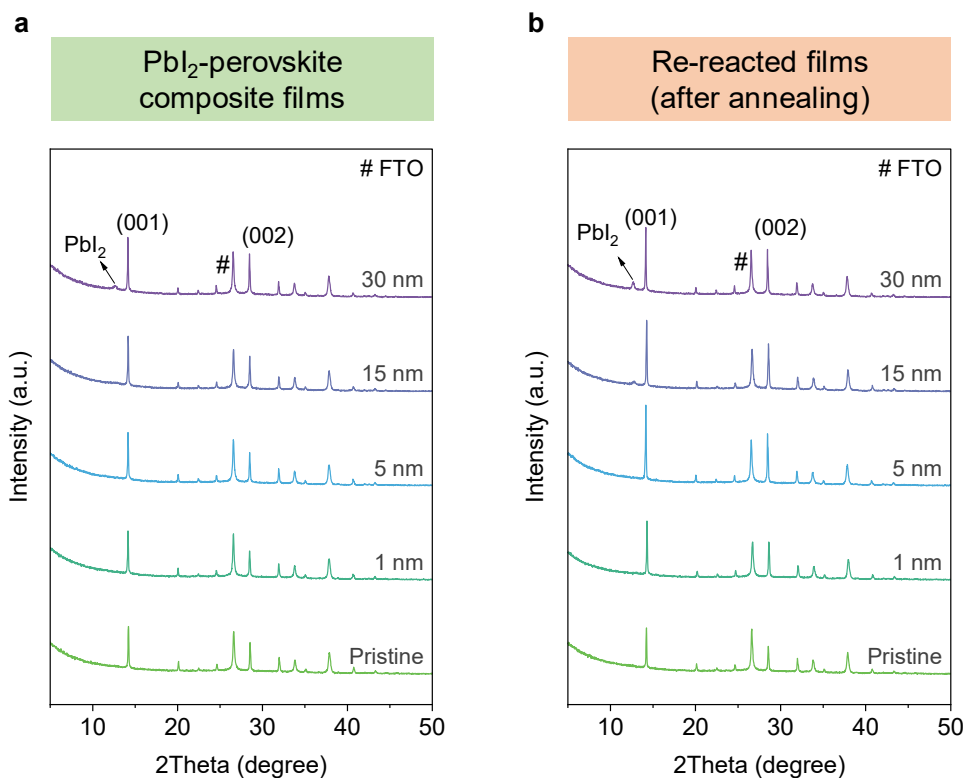


Fig. S5. (a) Pre-reaction and (b) re-reaction XRD patterns of pristine perovskite films, and SGR perovskite films with PbI_2 surface layers of varying thicknesses (1, 5, 15, 30 nm).

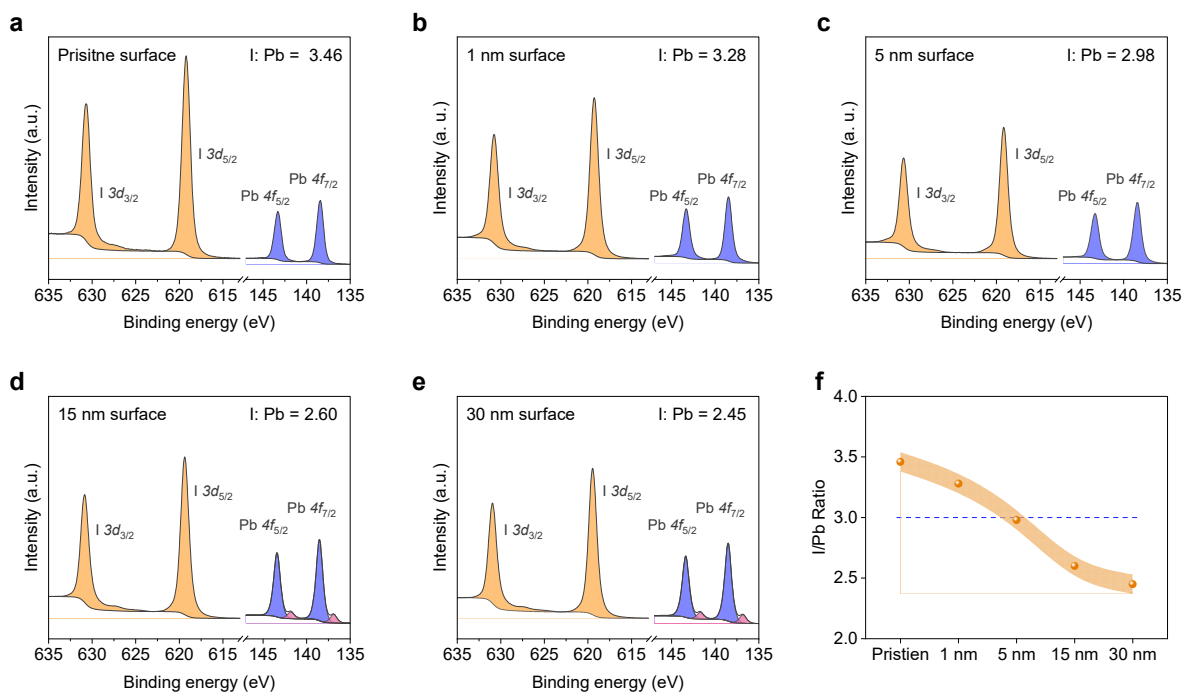


Fig. S6. High-resolution XPS spectra of re-reacted (a) pristine perovskite films and (b-e) SGR perovskite with PbI_2 surface layers of varying thicknesses (1, 5, 15, 30 nm). (f) I/Pb atomic ratio derived from XPS spectra.

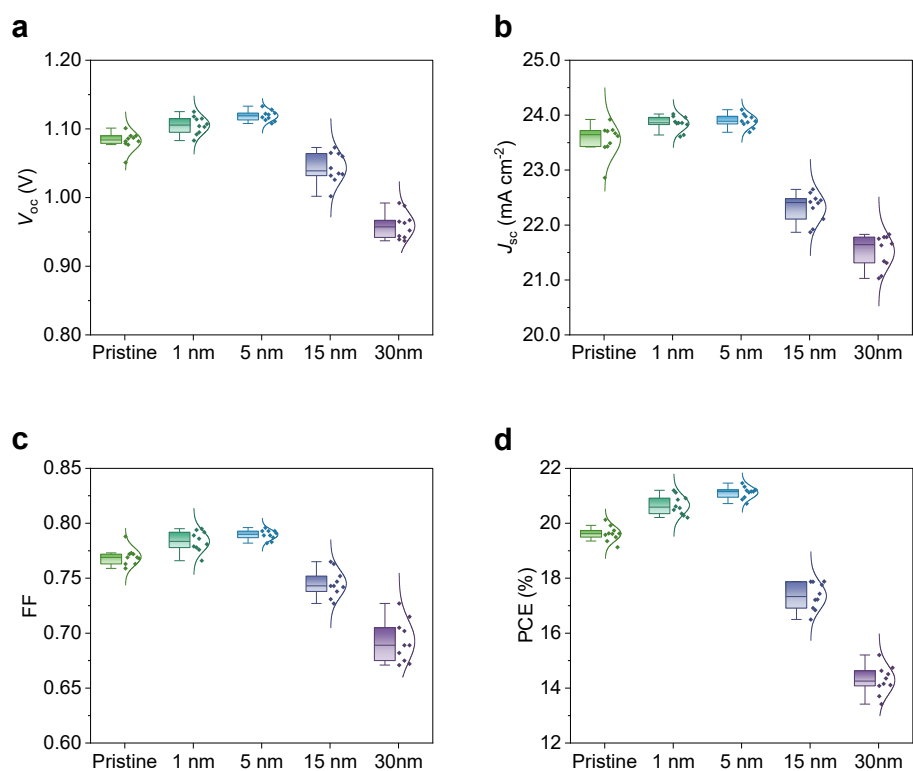


Fig. S7. Statistics of photovoltaic parameters distributions of pristine and SGR devices with PbI₂ surface layers of varying thicknesses (1, 5, 15, 30 nm).

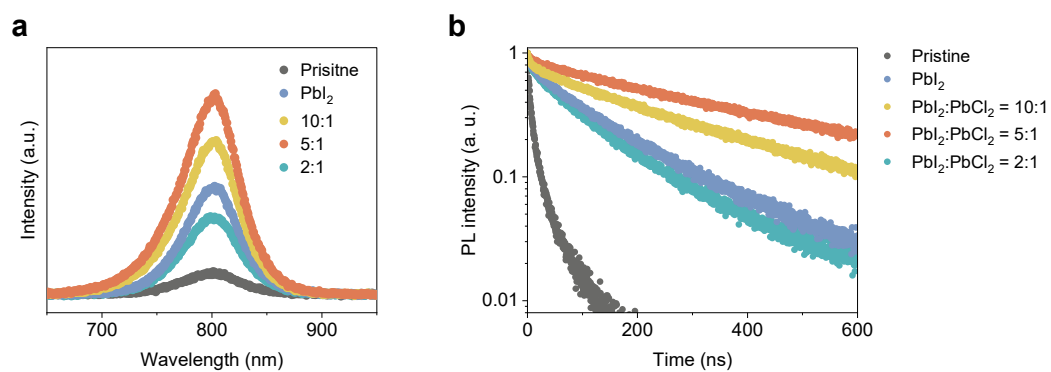


Fig. S8. (a) PL and (b) TRPL spectra of pristine perovskite and SGR perovskites with varying PbI₂/PbCl₂ ratios (including pure PbI₂).

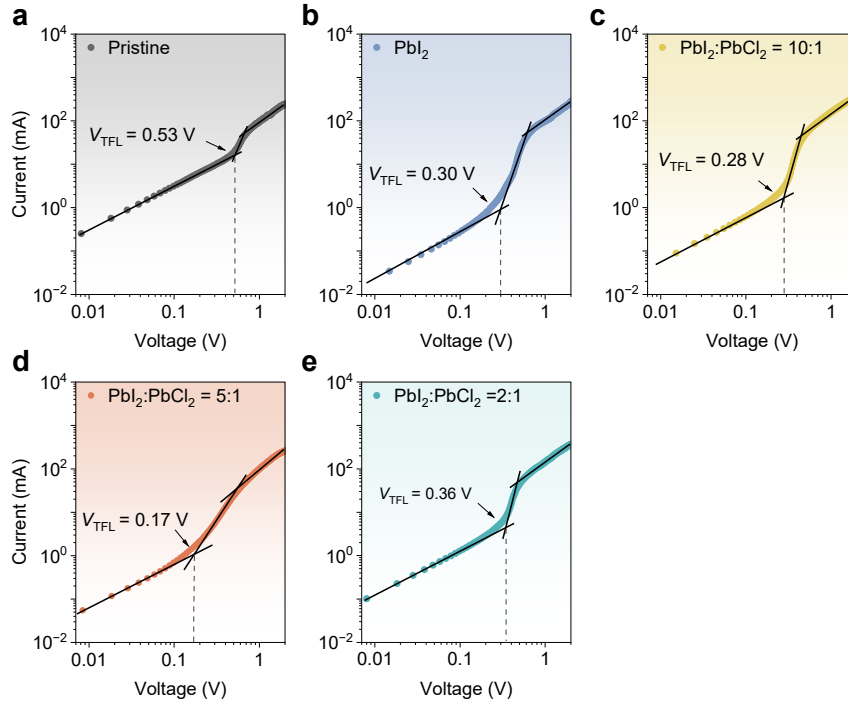


Fig. S9. SCLC analysis of (a) pristine, (b) pure PbI_2 SGR, and (c-e) SGR with varying $\text{PbI}_2/\text{PbCl}_2$ ratios electron-only devices. The structure of the devices is FTO/SnO_2 / perovskites/PCBM/Ag.

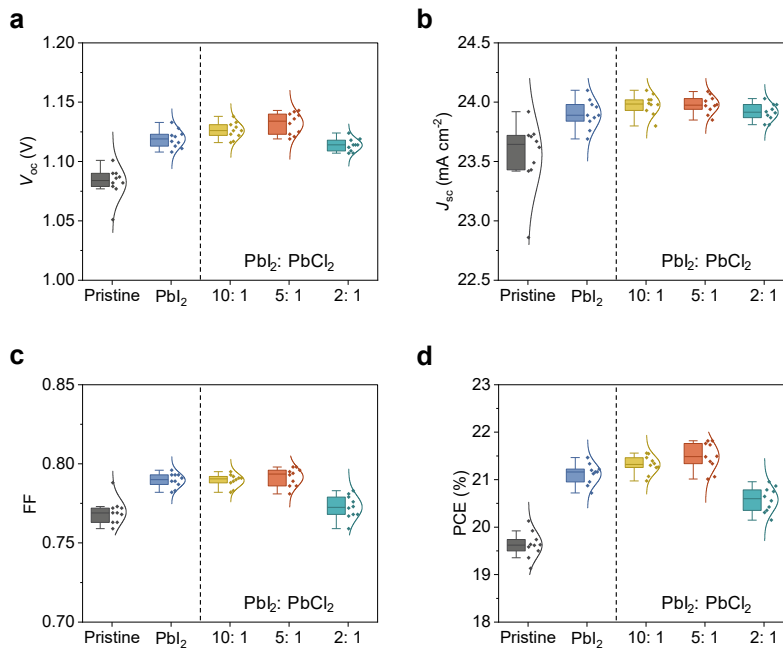


Fig. S10. Statistics of photovoltaic parameters distributions of pristine, pure PbI_2 SGR, and SGR with varying $\text{PbI}_2/\text{PbCl}_2$ ratios devices.

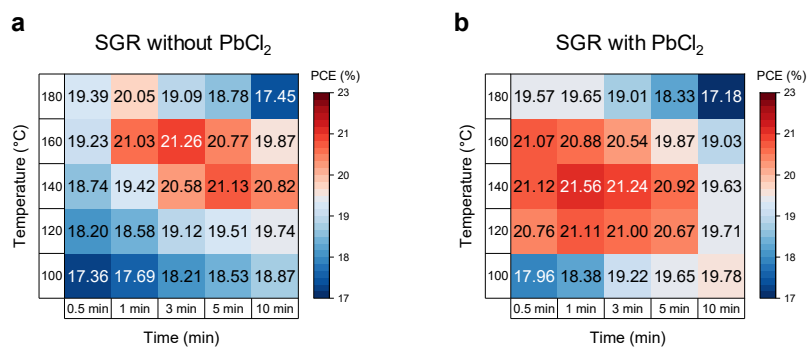


Fig. S11. Heatmaps of average PCE for SGR devices (a) without and (b) with PbCl₂ as functions of reaction time and temperature.

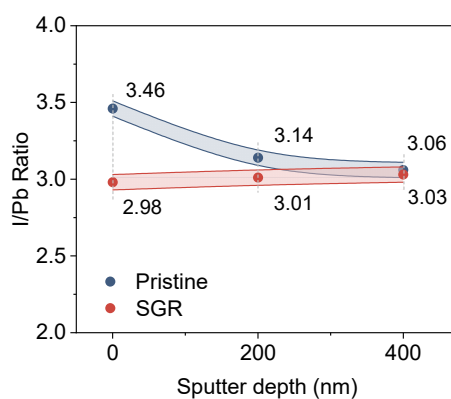


Fig. S12. Depth-dependent I/Pb ratio of pristine and SGR perovskite films, corresponding to Fig. 1e and Fig. 2d.

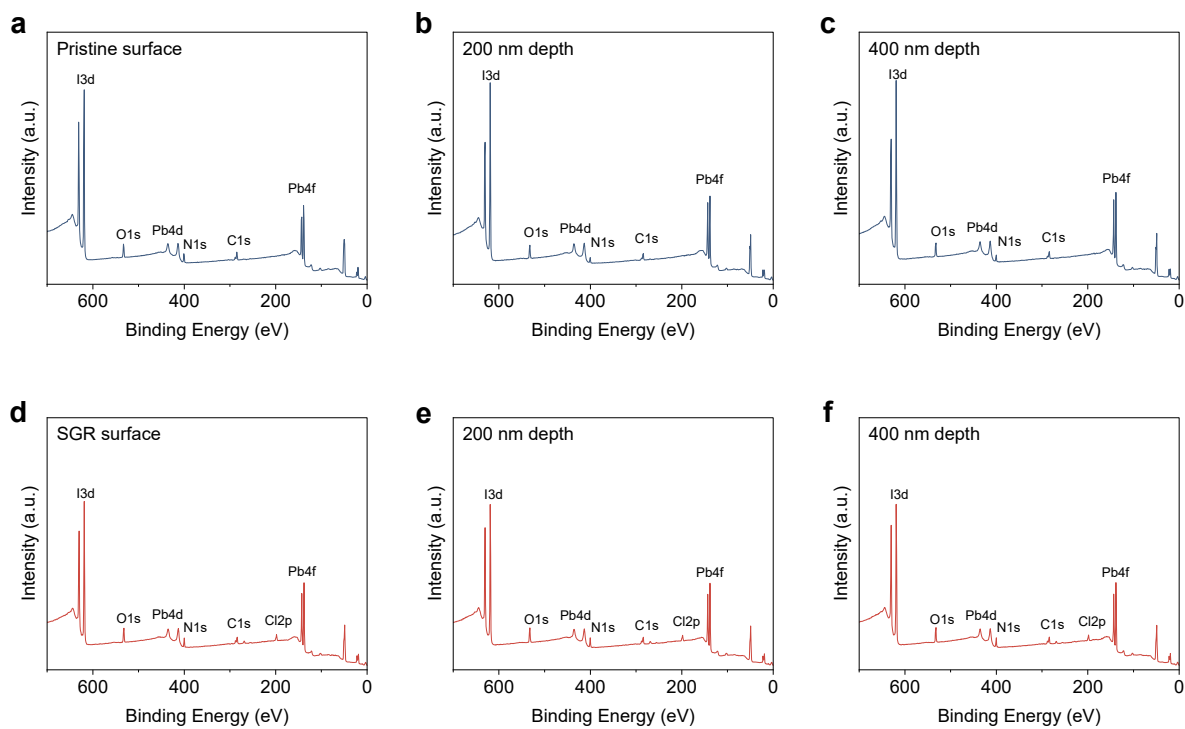


Fig. S13. XPS depth profiling Survey of (a-c) pristine perovskite and (d-f) SGR perovskite films.

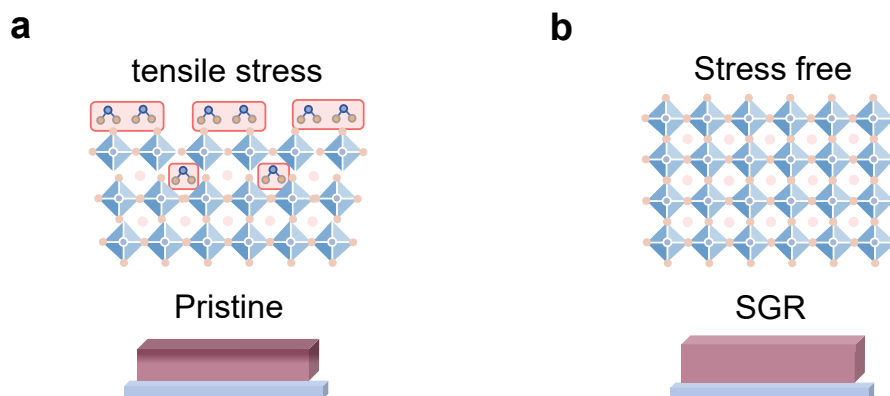


Fig. S14. Schematic illustrations of (a) tensile stress in pristine perovskite and (b) stress free in SGR perovskite.

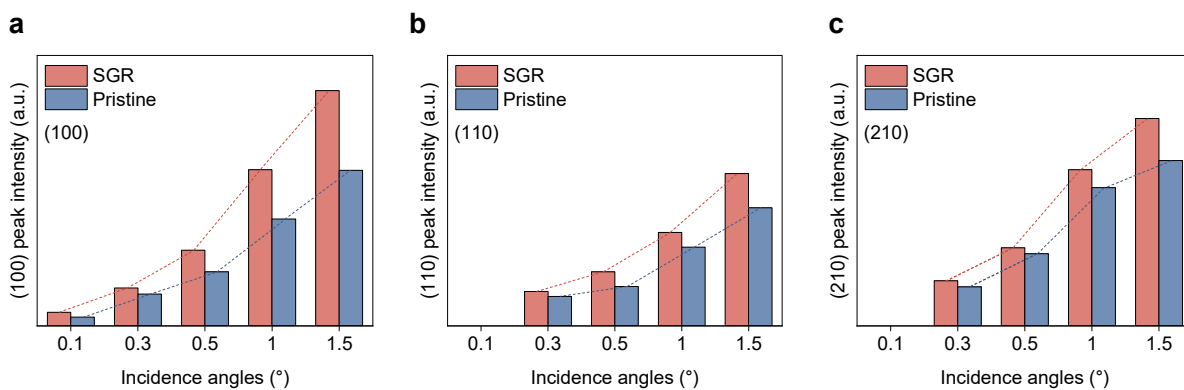


Fig. S15. Comparative GIXRD peak intensity analysis between pristine and SGR perovskites.

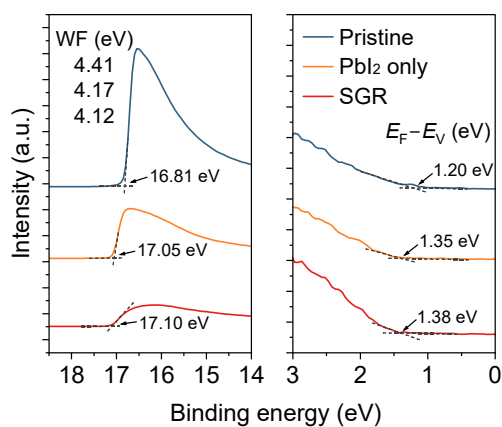


Fig. S16. UPS Spectra of pristine, PbI₂ only, and SGR perovskite films, corresponding to Fig. 3a.

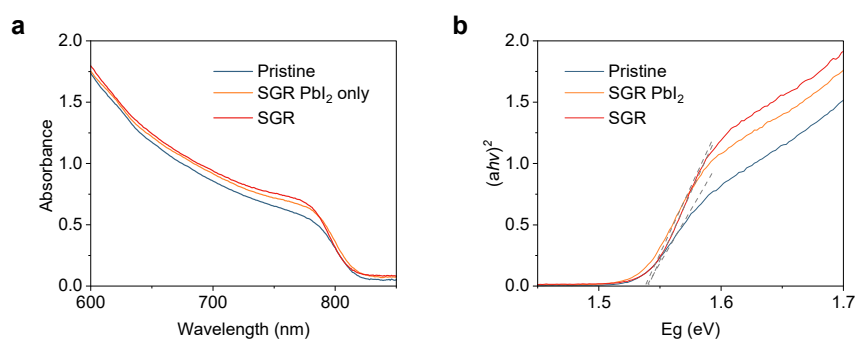


Fig. S17. (a) UV-Vis spectra and (b) Tauc plots of pristine, pure PbI₂ SGR, and SGR perovskite films.

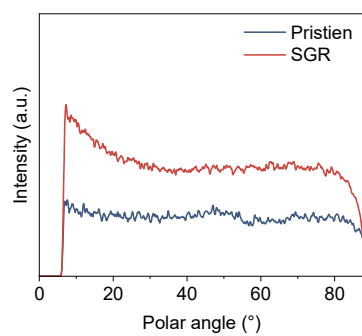


Fig. S18. Intensity azimuthal plot for the (001) rings of pristine and SGR perovskites, corresponding to Fig. 3d, e.

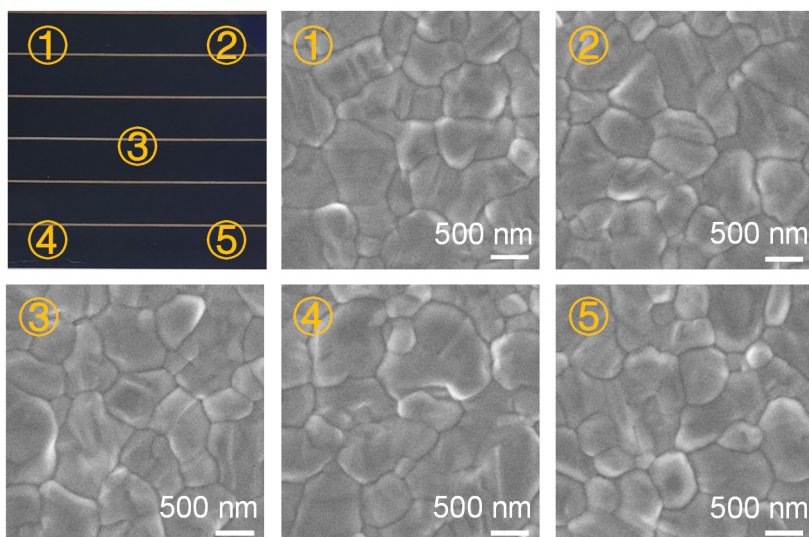


Fig. S19. SEM images of $5 \times 5 \text{ cm}^2$ large-area perovskite films.

Table S1. TRPL curve fitting results of pristine, PbI₂-SGR, and PbI₂/PbCl₂-SGR perovskite films, corresponding to Fig. S8.

Sample	A_1	τ_1 (ns)	A_2	τ_2 (ns)	τ_{avg} (ns) [*]
Pristine	0.74	3.69	0.26	27.32	20.75
PbI ₂ -SGR	0.30	7.78	0.70	151.55	148.46
10: 1-SGR	0.28	7.77	0.72	286.42	283.51
5: 1-SGR	0.20	10.77	0.80	413.26	410.65
2: 1-SGR	0.32	7.63	0.68	129.09	125.80

* τ_{avg} was fitted by the double-exponential equation: $\tau_{\text{avg}} = (A_1\tau_1^2 + A_2\tau_2^2)/(A_1\tau_1 + A_2\tau_2)$.

Table S2. TRPL curve fitting results of perovskite films, corresponding to Fig. 4b.

Sample	A_1	τ_1 (ns)	A_2	τ_2 (ns)	τ_{avg} (ns) [*]
Pristine	0.74	3.69	0.26	27.32	20.75
SGR	0.20	10.77	0.80	413.26	410.65

* τ_{avg} was fitted by the double-exponential equation: $\tau_{\text{avg}} = (A_1\tau_1^2 + A_2\tau_2^2)/(A_1\tau_1 + A_2\tau_2)$.

Table S3. The reported results of solar cells that prepare by vapor deposition. (Reverse scan)

Method	Area (cm ²)	V_{oc} (V)	J_{sc} (mA/cm ²)	Fill factor	PCE	Year	Ref.
	0.09	1.06	21.7	0.68	15.6		
	2.0	1.02	19.5	0.53	10.4		
Hybrid CVD	8.8	0.98	16.9	0.57	9.5	2016	4
	12	0.94	17.8	0.54	9.0		
	15.4	0.77	15.2	0.49	8.5		
Hybrid CVD	0.06	1.00	23.0	0.77	17.6	2016	5
Hybrid CVD	0.1	1.00	22.0	0.75	16.6	2018	6
	12.0	5.84	3.67	0.68	14.6		
Hybrid CVD	0.06	1.01	24.2	0.69	16.9	2018	7
	0.1	1.03	21.1	0.74	16.2		
Hybrid CVD	2.0	1.03	21.1	0.74	16.1	2019	8
	12.0	6.29	3.55	0.66	14.7		
Vapor-solid reaction	0.16	1.02	22.0	0.79	17.7	2019	9
	16.1	6.28	3.29	0.67	13.9		
Vapor-solid reaction	0.15	1.18	22.6	0.77	19.6	2020	10
	10.0	6.24	3.51	0.70	15.1		
Co-evaporation	0.09	1.08	21.7	0.78	18.3	2020	11
Vapor-solid reaction	0.15	1.13	22.2	0.78	19.6	2021	12
Vapor-solid reaction	0.15	1.07	23.8	0.80	20.5	2022	13
	10.0	6.50	3.95	0.67	17.0		
Sequential evaporation	0.10	1.15	25.9	0.82	24.4	2022	14
	14.4	6.72	4.2	0.70	19.87		
Hybrid CVD	0.09	1.15	23.93	0.80	21.98	2023	15
	22.4	7.82	2.91	0.71	16.16		
Hybrid CVD	1	1.079	23.13	0.79	19.60	2023	16
Vapor-solid reaction	10	6.61	4.12	0.69	18.78	2023	17
Vapor-solid reaction	1	1.12	23.27	0.79	20.06	2024	3
	10	6.71	3.77	0.76	19.41		
Sequential evaporation	64.8	10.25	1.95	0.75	15.01	2024	18
Solid-vapor reaction	12.4	5.43	4.42	0.77	18.4	2024	19
Solid-vapor reaction	0.148	1.14	24.29	0.81	22.45	2025	This work
	10	6.44	4.02	0.77	19.92		

References

1. L. Luo, Y. Zhang, N. Chai, X. Deng, J. Zhong, F. Huang, Y. Peng, Z. Ku and Y.-B. Cheng, *J. Mater. Chem. A*, 2018, **6**, 21143-21148.
2. T. Bu, J. Li, H. Li, C. Tian, J. Su, G. Tong, L. K. Ono, C. Wang, Z. Lin, N. Chai, X.-L. Zhang, J. Chang, J. Lu, J. Zhong, W. Huang, Y. Qi, Y.-B. Cheng and F. Huang, *Science*, 2021, **372**, 1327-1332.
3. C. Duan, J. Zhong, S. Hu, Y. Dou, J. Lu, Y.-B. Cheng and Z. Ku, *Adv. Funct. Mater.*, 2024, **34**, 2313435.
4. M. R. Leyden, Y. Jiang and Y. Qi, *J. Mater. Chem. A*, 2016, **4**, 13125-13132.
5. A. Ng, Z. Ren, Q. Shen, S. H. Cheung, H. C. Gokkaya, S. K. So, A. B. Djurišić, Y. Wan, X. Wu and C. Surya, *ACS Appl. Mater. Interfaces*, 2016, **8**, 32805-32814.
6. Y. Jiang, M. R. Leyden, L. Qiu, S. Wang, L. K. Ono, Z. Wu, E. J. Juarez-Perez and Y. Qi, *Adv. Funct. Mater.*, 2018, **28**, 1703835.
7. Q. Shen, A. Ng, Z. Ren, H. C. Gokkaya, A. B. Djurišić, J. A. Zapien and C. Surya, *ACS Appl. Mater. Interfaces*, 2018, **10**, 371-380.
8. Y. Jiang, M. Remeika, Z. Hu, E. J. Juarez-Perez, L. Qiu, Z. Liu, T. Kim, L. K. Ono, D.-Y. Son, Z. Hawash, M. R. Leyden, Z. Wu, L. Meng, J. Hu and Y. Qi, *Adv. Energy Mater.*, 2019, **9**, 1803047.
9. X. Deng, J. Hua, F. Huang, Y. Peng, W. Li, Z. Ku and Y.-b. Cheng, *Sustainable Energy Fuels*, 2020, **4**, 2491-2496.
10. L. Luo, Z. Ku, W. Li, X. Zheng, X. Li, F. Huang, Y. Peng, L. Ding and Y.-B. Cheng, *Sci. Bull.*, 2021, **66**, 962-964.
11. K. B. Lohmann, J. B. Patel, M. U. Rothmann, C. Q. Xia, R. D. J. Oliver, L. M. Herz, H. J. Snaith and M. B. Johnston, *ACS Energy Lett.*, 2020, **5**, 710-717.
12. C. Niu, C. Wang, G. Zhang, Q. Zhao, C. Fang, W. Li, F. Huang, Z. Ku and Y.-b. Cheng, *Sol. RRL*, 2021, **5**, 2100102.
13. G. Zhang, W. Luo, H. Dai, N. Li, Y. Li, Y. Peng, F. Huang, Z. Ku and Y.-B. Cheng, *ACS Appl. Energy Mater.*, 2022, **5**, 5797-5803.
14. H. Li, J. Zhou, L. Tan, M. Li, C. Jiang, S. Wang, X. Zhao, Y. Liu, Y. Zhang, Y. Ye, W. Tress and C. Yi, *Sci. Adv.*, 2022, **8**, eabo7422.
15. G. Tong, J. Zhang, T. Bu, L. K. Ono, C. Zhang, Y. Liu, C. Ding, T. Wu, S. Mariotti, S. Kazaoui and Y. Qi, *Adv. Energy Mater.*, 2023, **13**, 2300153.
16. Y. Qian, J. Li, H. Cao, Z. Ren, X. Dai, T. Huang, S. Zhang, Y. Qiu, L. Yang and S. Yin, *Adv. Funct. Mater.*, 2023, **33**, 2214731.
17. F. Tie, C. Duan, S. Hu, Y. Dou, Q. Tan, J. Fan, J. Lu, M. Xu and Z. Ku, *ACS Appl. Energy Mater.*, 2023, **6**, 6681-6688.
18. S. Zou, S. Liang, T. Yu, J. Su, Y. Jiang, R. Hua, Z. Huang, W. Zhang, L. Shi, Y. Guo, Q. Dong, Y. Han, H. Ma, Y. Gao, Y. Shi and Y. Dong, *Mater. Today Energy*, 2024, **40**, 101506.
19. D. Jiang, Z. Liu, J. Li, H. Cao, Y. Qian, Z. Ren, S. Zhang, Y. Qiu, C. Zhang, J. Wei, L. Yang and S. Yin, *Joule*, 2024, **8**, 1161-1175.